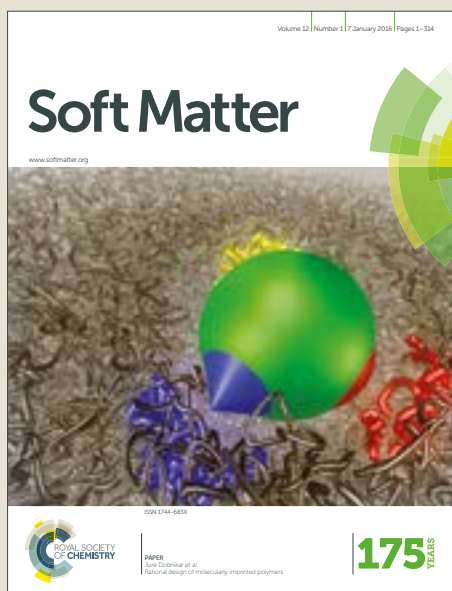


Soft Matter

Accepted Manuscript



This article can be cited before page numbers have been issued, to do this please use: M. Yang, R. Liu, F. Ye and K. Chen, *Soft Matter*, 2016, DOI: 10.1039/C6SM02516A.



This is an Accepted Manuscript, which has been through the Royal Society of Chemistry peer review process and has been accepted for publication.

Accepted Manuscripts are published online shortly after acceptance, before technical editing, formatting and proof reading. Using this free service, authors can make their results available to the community, in citable form, before we publish the edited article. We will replace this Accepted Manuscript with the edited and formatted Advance Article as soon as it is available.

You can find more information about Accepted Manuscripts in the [author guidelines](#).

Please note that technical editing may introduce minor changes to the text and/or graphics, which may alter content. The journal's standard [Terms & Conditions](#) and the ethical guidelines, outlined in our [author and reviewer resource centre](#), still apply. In no event shall the Royal Society of Chemistry be held responsible for any errors or omissions in this Accepted Manuscript or any consequences arising from the use of any information it contains.

Mesoscale simulation of phoretically osmotic boundary condition

Mingcheng Yang,^{1,2,*} Riu Liu,^{1,†} Fangfu Ye,^{1,2,‡} and Ke Chen^{1,§} View Article Online
DOI: 10.1039/C6SM02516A

¹*Beijing National Laboratory for Condensed Matter Physics and Key Laboratory of Soft Matter Physics, Institute of Physics, Chinese Academy of Sciences, Beijing 100190, China*

²*University of Chinese Academy of Sciences, Beijing 100049, China*

(Dated: December 5, 2016)

Boundary walls can drive a tangential flow of fluids by phoretic osmosis when exposed to a gradient field, including chemical, thermal or electric potential gradient. At microscales, such boundary driving mechanisms become quite pronounced. Here, we propose a mesoscale strategy to simulate the phoretically osmotic boundaries, in which the microscopic fluid-wall interactions are coarse-grained into the bounce-back or specular reflection, and the phoretically osmotic force is generated by selectively reversing the tangential velocity of specific fluid particles near the boundary wall. With this scheme, the phoretically osmotic boundary can be realized with a minimal modification to the widely used mesoscopic no-slip/slip hydrodynamic boundary condition. Its implementation is quite efficient and the resulting phoretically osmotic flow is flexibly tunable. Its validity is verified by performing extensive mesoscale simulations for both the diffusioosmotic and thermoosmotic boundaries. In particular, we use the proposed scheme to investigate fluid transport driven by the phoretic osmosis in microfluidic systems and the effects of the diffusioosmosis on the dynamics of active catalytic colloidal particles. Our work thus offers new possibilities to study the phoretically osmotic effect in active complex fluids and microfluidic systems by simulation, where the gradient fields are ubiquitous.

PACS numbers: 02.70.-c,47.11.-j,47.57.J-

I. INTRODUCTION

In simulations of the dynamics of complex fluids, a challenge is to bridge the enormous length- and time-scale gaps between the solvent and solute degrees of freedom [1, 2]. To treat this problem, considerable efforts have been made to develop mesoscopic fluid simulation methods including lattice Boltzmann [3], direct simulation Monte Carlo [4, 5], dissipative particle dynamics (DPD) [6–8], and multiparticle collision dynamics (MPC) [9–11]. By disregarding irrelevant microscopic details, these techniques correctly capture the essential physical features of the solvent, such as hydrodynamic interactions and thermal fluctuations. Mesoscopic fluid simulation methods thus provide access to length and time scales, where most of the relevant phenomena in complex fluids take place.

A complete mesoscale simulation must properly account for the hydrodynamic boundary condition between the solvent and the confinement, on which the dynamics of complex fluids sensitively depends. Two common boundary conditions are slip and no-slip boundaries [12], depending on the microscopic properties of the wall. At mesoscale level such boundary conditions can be modeled through simple collision rules between the solvent particles with the boundary, e.g., specular reflection for slip boundary [11, 13–15] and bounce-back operation for

no-slip boundary [16–18] (Fig. 1). The coarse-grained realization of the hydrodynamic boundary significantly reduces computational complexity.

Besides the no-slip and slip boundaries, another important type of hydrodynamic boundary is phoretically osmotic (PO) one [19–22] that is frequently encountered in the context of active colloids and microfluidics. The phoretic osmosis refers to the fluid motion along the boundary wall driven by the gradient fields parallel to the boundary. The driving gradients can be chemical, thermal and electric potential gradients, which correspond to diffusio-, thermo- and electroosmosis, respectively. Active colloids, which have attracted considerable interest during the last decade, often use the self-generated local gradients to produce self-propulsion [23–30]. The generated gradient, at the same time, can induce a tangential osmotic flow on the system boundaries, which in turn affects significantly the structure and dynamics of the active colloids [31–35]. On the other hand, owing to interfacially driven property, the phoretic osmosis is an efficient pumping mechanism on micro- and nanoscales, and has been widely used to manipulate fluids in microfluidic environment [36–39]. Therefore, a proper simulation realization of the PO boundary is critical for studies of active colloids, microfluidics and systems with gradient fields. Because the phoretic osmosis originates from microscopic interactions between the solvent molecule and the constituent atoms of the boundaries, in principle the PO boundary can be simulated by standard molecular dynamics method [40–44]. However, such microscopic realizations of the PO boundary are computationally too expensive to be feasible for large-scale simulations. Thus, a coarse-grained scheme for modeling the PO boundary

*Electronic address: mcyang@iphy.ac.cn

†Electronic address: lr@iphy.ac.cn

‡Electronic address: fye@iphy.ac.cn

§Electronic address: kechen@iphy.ac.cn

is highly desirable.

In this paper, we propose a mesoscale strategy to simulate the PO boundary. The microscopic interactions between the solvent and boundary are first coarse-grained into simple operations on the velocities of solvent molecules, either bounce-back or specular reflection. Then, a PO driving operation is introduced by reversing the tangential velocity of a specific type of solvent particles near the boundary wall. Here, the particle is classified in terms of its chemical species in the case of concentration gradient or its instantaneous kinetic energy in the case of thermal gradient. The selective reversion of the particle tangential velocity can lead to a PO force parallel to the boundary wall in inhomogeneous solutions. With this strategy, the implementation of the PO boundary is quite simple and efficient, similar to the case of the mesoscale no-slip/slip boundary. Moreover, the induced PO flow is a direct physical consequence of the interactions between the inhomogeneous solvent and the boundary, and is flexibly tunable. The proposed method is justified by means of mesoscale fluid simulations whose results are consistent with existing theoretical predictions. To demonstrate its applications, we use the method to simulate the PO-driven fluid transport in various microfluidic environments. The obtained results qualitatively agree with the previous molecular dynamics simulations or experiments. Furthermore, we study the effect of a diffusioosmotic boundary wall on the motion of an active colloidal sphere with a uniform catalytic surface. The simulation indicates that the diffusioosmotic flow can induce a strong accumulation or depletion of the colloidal particle at the wall, sensitively depending on the diffusioosmotic properties of the wall. The proposed mesoscale scheme thus provides us a promising tool to simulate the phoretic osmosis in active suspensions and microfluidic systems, and opens up new possibilities for mesoscale simulations of nonequilibrium complex fluids.

The paper is organized as follows. In Sec. II, the mesoscale scheme for modeling the PO boundary is introduced, where we limit ourselves to two typical phoretic osmosis: diffusioosmosis and thermoosmosis. In Sec. III, we describe the simulation approach and systems. Section IV presents the simulation results for both the diffusio-osmotic and thermo-osmotic boundaries. Finally, a conclusion is given in Sec. V.

II. PHORETICALLY OSMOTIC BOUNDARY CONDITIONS

Before explaining how to implement the mesoscale PO boundary condition, we briefly review the coarse-grained realization of the stick (no-slip) and slip hydrodynamic boundaries. For the stick boundary condition, the fluid velocity relative to the boundary is zero at the boundary surface. In most coarse-grained simulations, the stick boundary condition is achieved by the bounce-back rule [16–18, 45], in which the (relative) velocities of

the fluid particles are reversed upon a collision with the boundary, i.e., $\mathbf{v} \rightarrow -\mathbf{v}$, as shown in Fig. 1(a). Alternatively, the stick boundary can also be modeled stochastically [17, 46–48], where the tangential and normal velocities after a collision are taken from the Maxwellian-like distributions.

For the slip boundary condition, the tangential stress exerted on the boundary by the fluid is vanishing. The simplest way to implement the slip boundary condition is the specular reflection of the velocity of solvent particle at the boundary surface [15], namely reversing the normal component of the particle velocity at the point of collision, $v_n \rightarrow -v_n$ (Fig. 1(b)). Thus, the fluid momentum parallel to the boundary is conserved. Alternatively, a fluid particle-boundary potential interaction, which only depends on the normal distance between the boundary and the particle, also leads to the slip boundary condition [13, 14].

Different from the stick and slip boundaries, the PO boundary is a driving boundary, arising from interactions between the boundary wall and the inhomogeneous solution induced by gradient fields. An intuitive picture of the phoretic osmosis can be described as the following. In a quiescent fluid, each fluid particle may transfer a tangential momentum to the boundary by collision, and exert an instant tangential force on the boundary. The direction of the instant tangential force distributes isotropically in a homogeneous fluid, hence the mean tangential force on the boundary vanishes. In contrast, in a gradient-induced inhomogeneous fluid, the momentum transfers along and against the gradient direction may not cancel each other due to inhomogeneous fluid-boundary interactions. This results in a nonzero mean tangential force parallel to the gradient, which is the driving force of the phoretic osmosis. The phoretically osmotic force accelerates the fluid from the boundary, and is balanced by the hydrodynamic frictions in a steady-state flow. Thus, to properly model the PO boundary condition, two essential requirements are the tangential

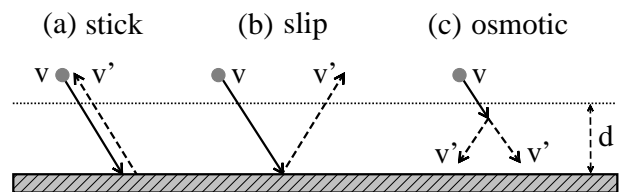


FIG. 1: Schematic hydrodynamic boundary conditions. No-slip (a) and slip (b) boundaries are realized separately by bounce-back operation and specular reflection of the velocity of the fluid particle upon a collision with the wall surface. (c) Phoretically osmotic boundary is implemented by conditionally reversing the tangential velocity of the fluid particle within the fluid-boundary interaction range marked by dotted line. At the same time, the bounce-back rule or specular reflection is applied at the wall surface. \mathbf{v} and \mathbf{v}' refer to the fluid particle velocities before and after the operation of velocity, respectively.

momentum transfer and the inhomogeneous interactions between the fluid and the boundary.

At mesoscales, tangential momentum transfer can be easily implemented by a stick-like collision rule between the fluid particle and the boundary, e.g., the bounce-back rule. On the other hand, the inhomogeneous interactions induced by gradient fields imply that the solvent particles with different features (e.g. the particle species for chemical gradient) interact differently with the boundary. From the above argument, the diffusio-osmotic boundary condition in a fluid consisting of two components can be straightforwardly modeled by performing the bounce-back operation for one species and the specular reflection for the other species upon a collision with the boundary. This simple scheme may indeed generate an osmotic flow along a concentration gradient parallel to the boundary (not shown). But, the diffusio-osmotic flow thus produced is too weak for a simulation application, and is not flexibly tunable once the concentration gradient is given. The weak PO flows are due to the short range of interaction between the solvent and the boundary.

To enhance the tangential coupling between the fluid and the boundary, and hence the PO flow, we introduce a parameter, d , to re-define the fluid-boundary interaction range. Specifically, we consider the diffusio-osmotic boundary in a fluid including A and B components. First, both A and B particles experience the same type of collision at the boundary surface, either the bounce-back operation or the specular reflection, corresponding to the common stick or slip boundaries, respectively. Second, particles of species A locating within the interaction range d with the normal velocities pointing to the boundary reverse their tangential velocities, $\mathbf{v}_\tau \rightarrow -\mathbf{v}_\tau$. The second step, which we name the ‘‘driving operation’’, is sketched in Fig. 1(c). The driving operation greatly enhances the tangential momentum transfer between the fluid and the boundary. As a consequence, a stronger diffusio-osmotic flow can be produced along the gradient of A component. Moreover, the magnitude of the flow can be tuned by changing the interaction range d . And, an opposite osmotic flow (i.e. along the gradient of B component) can be obtained by performing the driving operation for B component instead of A component.

Following the above procedure the thermoosmotic boundary can be similarly implemented. For a single-component nonisothermal fluid, its inhomogeneity is reflected in the instantaneous kinetic energy of the fluid particle, E_i . The fluid particles in high temperature area are more possible to have large E_i . So, in order to selectively perform the driving operation for the fluid particles, as in the diffusioosmotic case, we impose a threshold temperature, T_t , to classify the fluid particles. The particle with $E_i < 1.5k_B T_t$ (k_B being the Boltzmann constant) is called as the cold-particle, otherwise as the hot-particle. When the driving operation is performed for the hot-particles, the resulted thermoosmotic flow will be along the thermal gradient, since there are more hot-particles in high temperature area; otherwise

the flow will be against the thermal gradient. For the thermoosmotic boundary, the flow velocity can be regulated by both parameters T_t and d . View Article Online
DOI: 10.1039/C6SM02516A

Thus, with minimal modifications to the implementation of the coarse-grained no-slip or slip boundary conditions, we are now able to realize the mesoscale PO boundary conditions in simulations. In the following sections, we verify the validity of the proposed scheme by performing extensive mesoscopic fluid simulations. In the simulations we use the multi-particle collision dynamics method (MPC) to describe the fluid, although our PO boundary conditions can be implemented similarly in other mesoscale simulation approaches.

III. SIMULATION METHOD AND SYSTEMS

A. MPC fluid

In the MPC method, the fluid is represented by N point particles, with the mass m , position \mathbf{r}_i , and velocity \mathbf{v}_i of particle i , $i \in \{1, \dots, N\}$. The particle dynamics consists of alternating streaming and collision steps. In the streaming step, the fluid particles move ballistically for a time step h ,

$$\mathbf{r}_i(t+h) = \mathbf{r}_i(t) + h\mathbf{v}_i(t). \quad (1)$$

In the collision step, particles are sorted into a cubic lattice with cells of size l_c , and their velocities relative to the center-of-mass velocity of each cell are rotated by a fixed angle α around a randomly oriented axis [9–11, 13]. These are described by the velocity update

$$\mathbf{v}_i(t+h) = \mathbf{v}_{cm}(t) + \mathbf{\Omega}(\mathbf{v}_i(t) - \mathbf{v}_{cm}(t)), \quad (2)$$

where \mathbf{v}_{cm} is the center-of-mass velocity of the collision cell and $\mathbf{\Omega}$ is the rotational matrix. In order to guarantee Galilean invariance, the grid of collision cells is randomly shifted at each time step [49]. In the coarse-grained collision, mass, momentum, and energy are locally conserved, which assures the algorithm to properly capture hydrodynamic interactions, mass transport, and heat conduction. Moreover, thermal fluctuations are naturally involved in this algorithm. Note that the driving operation within the boundary layer that generates the PO flow is performed after each MPC collision step, such that it is independent of the particle sorting and the random shift of collision cells.

In simulations, lengths are measured in units of l_c , energies in units of $k_B T$ (for convenience the Boltzmann constant k_B is set as 1), and masses in units of m . This corresponds to setting $m = 1$, $l_c = 1$, and $T = 1$. Here, we employ the MPC parameters $\alpha = 120^\circ$, $h = 0.1$, and the mean number of fluid particles per cell $\rho = 10$, which produces a liquid-like dynamics with a Schmidt number $Sc \simeq 13$.

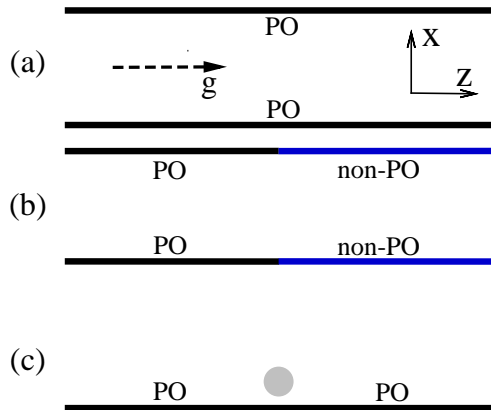


FIG. 2: Schematic diagram of the simulation systems where the PO boundaries are studied. Here, the periodic boundary conditions are employed in y and z directions. (a) Both the walls of the channel have the PO boundary condition and the gradient field is absent. (b) The left half and right half sides of the channel have the PO boundary and the common stick/slip boundary, respectively. The gradient field is along the z axis and symmetric with respect to the middle of the channel. (c) A semi-infinite fluid is confined by a bottom wall. The gray sphere refers to a fixed active fluid region (chemical or heat source) or a moving colloidal sphere with a uniform catalytic surface.

B. Systems

In simulations we implement both the diffusioosmotic and thermoosmotic boundary conditions. For each type of PO boundary, we study three different cases. First, we consider a homogeneous (zero gradient) fluid in a channel with the PO boundary condition in x direction and the periodic boundary condition in other directions, with an external force g along the z axis being exerted on every fluid particle, as plotted in Fig. 2(a). Such a system allows us to test whether in the absence of gradient fields the PO boundary condition can lead to a stick-like boundary, since the driving operation in the PO boundary produces a tangential momentum transfer within the boundary layer. Second, we simulate a fluid confined in a narrow channel with the PO boundary condition applied in the left half channel and the common stick/slip boundary condition in the right half channel, as sketched in Fig. 2(b). A symmetric gradient field is imposed with respect to the middle of the channel in the z direction. Thanks to the heterogeneous boundaries, the symmetric gradient will drive a directed flow along the channel, acting as a microfluidic pump. Based on this configuration, we investigate the dependence of the PO flow on the system parameters, such as the interaction length d and the field gradient. Third, we simulate the phoretic osmosis driven by a single boundary wall in a ‘semi-infinite’ fluid, in which the gradient fields are generated by a small fluid region fixed near the wall, i.e., chemical or heat source (see Fig. 2(c)). In actual simulations we still consider two walls in x -direction, but with the wall-separation much

larger than that in Fig. 2(b). Thus, the distant wall hardly produces a PO flow since the field gradient near that wall is negligibly small. This configuration is relevant for microfluidics, where the gradient fields are often created by local sources. Furthermore, in order to study the effect of the PO boundary in active colloids, we simulate a colloidal particle with a uniform catalytic surface moving near a diffusioosmotic wall (also see Fig. 2(c)).

IV. RESULTS AND DISCUSSIONS

A. Diffusioosmotic boundary

1. Homogeneous fluid under an external force

The simulation system is sketched in Fig. 2(a), with the sizes $L_x = L_y = 16$ and $L_z = 40$, and the external force on each particle $g = 0.0001$. The confined fluid consists of equimolar A and B components. The PO boundary condition is implemented by combining the bounce-back collision at the wall surface and the driving operation for A particles within the interaction range, $d = 0.5$. Due to the absence of the gradient fields, the driving operation only contributes to the friction between the fluid and the boundary. In the steady state, the external force results in a parabolic flow, as shown in Fig. 3(a). The extrapolation of the flow velocity to the wall gives a vanishing surface velocity, which shows that the PO boundary condition in a homogeneous fluid produces a good stick-like boundary.

It is known that the simple bounce-back rule can not reproduce a strictly stick boundary in the MPC fluid due to partially filled collision cells at the boundaries induced by the random shift, and requires modifications by introducing virtual wall particles [16]. In the present simulations, both the bounce-back and the driving operations contribute to the fluid-wall friction, such that the boundary is more sticky than that realized only with the simple bounce-back rule. Note that throughout the present work the virtual wall particles are not used. We emphasize that the partially filled cells does not affect the PO driving operation in our method, since by construction the driving operation is implemented after the collision step for fluid particles near the wall, independent of the collision cell and its random shift.

With the maximum velocity of the parabolic flow v_{max} , we can determine the shear viscosity of the fluid using the relation, $\eta = g\rho L_x^2/8v_{max}$ [50, 51]. The obtained viscosity is $\eta = 8.4$, in a good agreement with the value 8.7 obtained from kinetic theories [52].

2. Inhomogeneous fluid in a heterogeneous channel

The system in Fig. 2(b) has the dimensions $L_x = L_y = 10$ and $L_z = 40$, with the PO boundary only for the left half channel. The symmetric concentration gradient ∇c

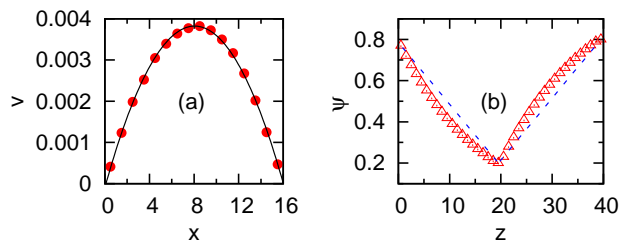


FIG. 3: (a) Poiseuille flow of a homogeneous binary fluid in a channel with the diffusioosmotic boundary. The lines correspond to parabolic fits to the flow profile. (b) Steady-state molar fraction profile of A component in a heterogeneous channel with the left half side having the diffusioosmotic boundary of $d = 0.5$. The driving operation is performed for A particles, producing an osmotic flow against the z direction. The dashed lines refer to the molar fraction distribution in a quiescent fluid.

in the z direction is generated by fixing the concentration of species A at $L_z/2$ and L_z , where reaction $A \rightarrow B$ and $B \rightarrow A$ take place respectively. The reactions are performed by directly transforming the particle species in local areas with an imposed probability, by which the concentration gradient is tuned. Such a simple reaction scheme has been widely used in mesoscale simulations of self-diffusiophoretic microswimmers [18, 26, 27, 45] and micromachines [30, 44]. Although A and B particles both take part in the same MPC collision, they are physically distinguishable by their different interactions with the boundary wall. Because the mass is locally conserved in the MPC fluid, the mass diffusion can be correctly captured within the solution. Under the resulted chemical gradient, the diffusioosmosis driven by the left-side boundaries causes a directed fluid flow through the channel. Although the reaction operation in the simulations does not input external energy into the system, it continuously decreases the system entropy by changing the particle species in the reaction areas such that the system is kept out-of-equilibrium. In the presence of concentration gradient generated by the chemical reaction, our simulations satisfy the first law of thermodynamics, as the total energy of system (including the internal energy and the kinetic energy of macroscopic fluid flow) is conserved. The kinetic energy of macroscopic flow is extracted from the system internal energy through the diffusio-osmotic effect; meanwhile the macroscopic kinetic energy is dissipated into the internal energy by friction. The system reaches the steady state when these two processes balance each other. Moreover, the extraction of the directed transport from the system internal energy does not violate the second law of thermodynamics, since the system in our simulation is non-equilibrium.

In the simulations, the parameters d and ∇c are adjusted, and the driving operation is separately applied for species A and B to obtain opposite PO flows. Figure 3(b) plots a typical steady-state concentration distribution of A component, which slightly deviates from the expected linear profile for a quiescent fluid. This deviation arises

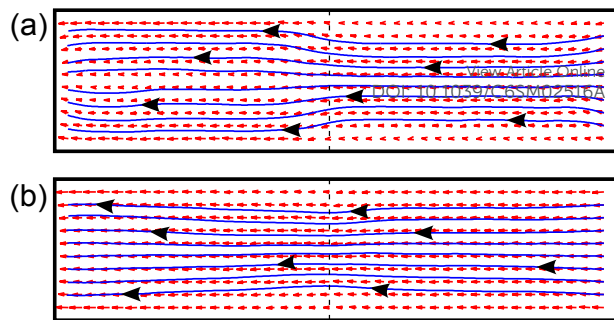


FIG. 4: Cross-section of the flow fields of an inhomogeneous binary fluid in a heterogeneous channel with the diffusioosmotic boundary conditions. (a) corresponds to type-I boundary and (b) to type-II. Here, $d = 0.5$, the concentrations fixed at $L_z/2$ and L_z are the same as those of Fig. 3(b), and the driving operation is performed for A component. The dashed line is the dividing line between the driving (left) and passive (right) parts of the channel. Small red arrows indicate the flow velocity direction and intensity, while the blue lines refer to the streamlines.

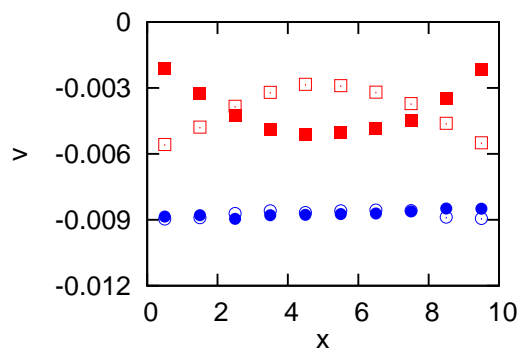


FIG. 5: Velocity profiles for the flows in Fig. 4. Open and close symbols separately refer to the flow velocities in the middle sections of the driving ($z = L_z/4$) and passive ($z = 3L_z/4$) parts of the channel. Squares and circles correspond to Fig. 4(a) and (b), respectively. Here, the positive direction of the flow velocity is defined to be along the z axis.

es from the PO boundary-induced convective flows, and can be understood by considering the total flux equation $j = -D_s \nabla c(z) + c(z)\mathbf{v}$, with D_s and \mathbf{v} being the diffusion coefficient of the fluid particles and the convective flow velocity, respectively. In the steady state, j is a constant. Assuming that D_s and \mathbf{v} are position-independent, larger convective flow (i.e. higher c) will accompany stronger diffusive flow (i.e. larger ∇c), if they have opposite direction; otherwise the situation will reverse, as shown in Fig 3(b). We point out that in a real liquid the PO-induced flow velocity is generally very small relative to the diffusive flow velocity, so the concentration would be linear with position. However, in the present mesoscale fluid the ratio between the diffusive and convective characteristic times is around $l_c v / D_s \sim 10^{-1}$, larger than the real case.

Figure 4 shows a typical diffusioosmosis-induced flow

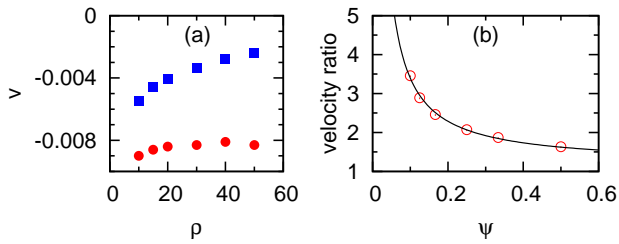


FIG. 6: (a) Diffusioosmotic flow velocity as a function of the mean total number density of fluid particles (including A and B). Squares and circles correspond to type-I and type-II boundaries, respectively. Here, the mean number density of A particles remains fixed, $\rho_A = 5$, and the concentration gradient of A component keeps unchanged, with the same value as that in Fig. 4. (b) Flow velocity ratio of type-II to type-I as a function of molar fraction of species A. The line refers to a fit (see main text).

field in the heterogeneous channel. Here, we consider two different implementations of the diffusioosmotic boundary condition: (I) the bounce-back rule plus the driving operation (Fig. 4(a)) and (II) the specular reflection plus the driving operation (Fig. 4(b)). The bounce-back rule or the specular reflection is applied at the wall surface of the whole channel; while the driving operation is only performed in the left half channel. Obviously, the type I and II correspond to the no-slip and slip limit of the PO boundary, respectively. Their stationary flow fields are very different, which becomes clear by comparing the velocity profiles of the fluid, as plotted in Fig. 5. Particularly, the velocity profiles for the driving and passive sides are significantly different in case I, however they are very similar in case II. An intuitive explanation is that the driving and passive parts of the type-I boundary are respectively slip-like and stick-like; while for the type-II both parts have slip-like boundaries.

Regarding the above two diffusioosmotic implementations, an interesting question is how much flow enhancement can be obtained with type-II boundary relative to type-I? We investigate this question by comparing the flows in Fig. 4(a) and (b). In our simulations, the friction arises mainly from B component for type-I boundary and completely from A component for type-II boundary. Consequently, when fixing the concentration of A species and its gradient (hence driving force), the flow velocity for type-I boundary is inversely proportional to the total number density of the fluid particles, while for the type-II boundary, the flow velocity is insensitive to the total number density. This agrees with the simulation results in Fig. 6(a). Note that the osmotic flow velocity for the type-II boundary in Fig. 6(a) has a small (but measurable) dependence on the total number density ρ , slightly decreasing with ρ and saturating at larger densities. This weak dependence arises from the fact that the solvent diffusion coefficient slightly depends on the total density through $\rho/(\rho-1)$ [52]. Since the driving operation simply reverses the tangential velocity of A-particles within the

boundary layer, the diffusioosmotic driving force is determined by the diffusive flow of A-particles in the boundary layer, hence proportional to the concentration gradient, the diffusion coefficient and the interaction length. For fixed ∇c and d , the relation between the diffusion coefficient and ρ explains the slight dependence of the flow velocity on ρ .

Thus, the velocity ratio of type-II to I is inversely proportional to the molar fraction of species A, namely $\sim 1/\Psi$. Figure 6(b) plots the ratio as a function of Ψ , which can be well fitted by the function of $a/\Psi + b$. Most experiments are performed at low chemical concentrations. We can thus extrapolate the velocity ratio to this regime using the fitted function. For a concentration $\sim 0.01M$ of A component, the velocity ratio is around 1000, which is a giant amplification. The present results are consistent with previous MD simulations and theoretical calculation [40, 41], which predicted that the diffusioosmotic flows at slip surfaces can be massively amplified by 2 to 3 orders of magnitude compared to no-slip surfaces.

In the following we focus on type-I boundary and investigate the dependence of the diffusioosmotic flows on ∇c and d . Figure 7(a) indicates that the flow velocity is linearly proportional to the applied ∇c , consistent with the well-known theoretical prediction in linear response framework [19]. The linear flow-gradient relation is the most essential feature of phoretic osmosis, so the result in Fig. 7(a) constitutes a strong evidence that the present mesoscale scheme can properly model the diffusioosmosis. Figure 7(b) shows that for fixed ∇c the flow velocity also sensitively depends on d ; the flow velocity increases with d until it saturates at larger d . For the mesoscopic diffusioosmotic boundary, this dependence on d is the result of balance between the diffusioosmotic force f_D and the hydrodynamic friction f_F . The diffusioosmotic force originates from the total momentum change of A-particles within the boundary layer during the driving operation in a quiescent fluid, and hence is proportional to the concentration gradient and the interaction length d , namely $f_D \propto d\nabla c$, as mentioned above. On the other hand, the frictional force arises from the momentum change of the macroscopic flowing fluid due to the fluid-wall couplings, including the bounce-back at the wall surface and the driving operation within the boundary layer. The friction from the bounce-back is proportional to the convective flow velocity v ; while the friction from the driving operation depends on both v and d that effectively measures the number of A-particles interacting with the boundary in the driving operation. Thus, the total friction can be expressed as $f_F \sim -(\gamma_B v + d\gamma_D v)$, with γ_B and γ_D denoting the bounce-back friction coefficient and the driving operation-induced friction coefficient per unit thickness, respectively. By force balance, the diffusioosmotic flow velocity reads $v \sim \nabla c/(\gamma_B/d + \gamma_D)$, which explains the simulation results in Fig. 7 very well. Furthermore, for the same ∇c and d , by implementing the driving operation for species B instead of A, the generat-

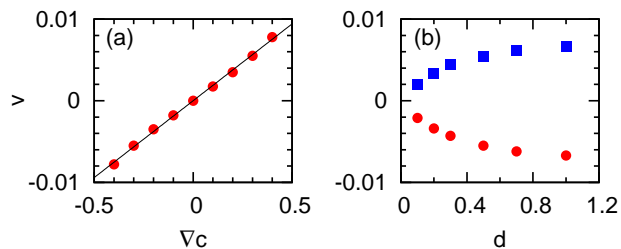


FIG. 7: Diffusioosmotic flow velocity as a function of (a) the concentration gradient of species A with $d = 0.5$, and (b) d with $\nabla c = -0.03$. Here, circles and squares respectively refer to the driving operation applied for A and B particles, and line is a linear fit.

ed diffusioosmotic flow reverses, which corresponds to the wall materials with opposite diffusiophoretic properties. These results also indicate that the mesoscale diffusioosmotic boundary is flexibly tunable.

3. Inhomogeneous fluid driven by a single wall

We now apply the mesoscale diffusioosmotic boundary in the simulations relevant to active suspensions and microfluidics, as sketched in Fig. 2(c). A spherical region of active fluid with radius 0.8 near the wall continuously releases chemicals, creating a radially symmetric concentration gradient in the planes parallel to the wall. To maintain a steady-state gradient, the released chemicals is consumed in the areas far from the active region. This scenario is realized in the simulation by performing reaction $A \rightarrow B$ within the active region and reaction $B \rightarrow A$ beyond a large distance from the active region. The system sizes are $L_x = L_y = L_z = 40$ with wall boundary in the x direction and periodic boundary for other directions, and the separation between the bottom wall and the center of the active region is 2.0. Here type-I diffusioosmotic boundary is used, with an interaction range of $d = 0.5$. Figure 8(a) and (b) display the stationary concentration distribution on the plane of $x = 0.5$. The induced gradient component parallel to the wall drives a radial symmetric diffusioosmotic flow with respect to the chemical source along the wall, as shown in Fig. 8(c) and (d). When the driving operation is applied to species A, the osmotic flow points away from the chemical source near the wall, and is compensated by inward flows from the bulk solution (Fig. 8(c)), forming vortex structures. The flow patterns are reversed when the driving operation is applied to species B (Fig. 8(d)). In Fig. 8(e), the diffusioosmotic flow velocity at $x = 0.5$ is displayed as a function of the in-plane distance to the center of the active region, which has a maximum in the vicinity of the active region and decays to zero at a distance where the concentration gradient is vanishing. We point out that this simple configuration nicely mimics the recent experiments by McDermott *et al* [38]. In that work, a calcium carbonate particle fixed on the substrate surface in an un-

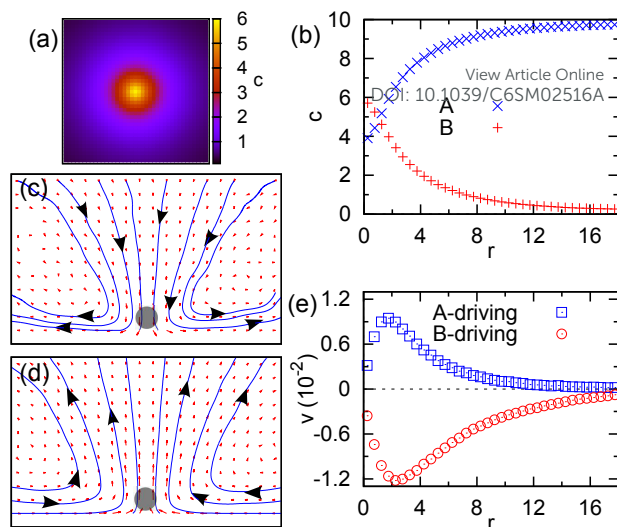


FIG. 8: Concentration and flow fields induced by a chemical source close to a wall with the diffusioosmotic boundary condition. (a) Concentration map of species B on the plane of $x = 0.5$ and (b) the corresponding concentration as a function of the in-plane distance to the chemical source center. (c) and (d) refer to the flow fields on the yz plane across the source center, where the driving operations are performed for A particles and B particles, respectively. Here, the gray circles represent the active sources. (e) Flow velocity as a function of the in-plane distance to the active source on the plane of $x = 0.5$. Here the squares and circles correspond to the flows in (c) and (d), respectively. The positive velocity is directed outwards from the active source.

saturated aqueous solution drives a diffusioosmotic flow along the substrate due to self-generated chemical gradients, and the resulting flow field agrees well with our simulation.

4. Catalytic colloidal sphere near a diffusioosmotic wall

The diffusioosmotic wall is expected to have an important effect on the dynamics of active catalytic colloid, which catalyzes chemical reaction in solutions to generate local chemical gradients. To investigate this effect, we consider a neutrally buoyant colloidal sphere with a uniformly catalytic surface that moves freely in a binary solvent consisting of A and B components. Similar to the system of Fig. 2(c), the solution is confined by the walls in x direction with $L_x = 26$ and has the periodic boundary conditions in other directions with $L_y = L_z = 40$. The colloidal sphere interacts with both A and B solvent particles through the same repulsive Lennard-Jones-type (LJ) potential,

$$U(r) = 4\epsilon \left[\left(\frac{\sigma}{r} \right)^{48} - \left(\frac{\sigma}{r} \right)^{24} \right] + \epsilon. \quad (3)$$

Here, the potential intensity $\epsilon = k_B T$ and the radius of colloidal sphere $\sigma = 2.5a$ are used with the cutoff radius

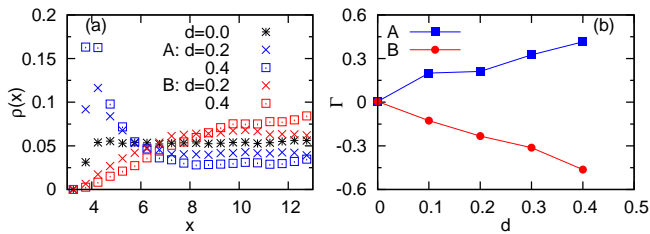


FIG. 9: (a) Probability density $\rho(x)$ to find the colloidal sphere at a distance x from the wall. Here, A and B refer to the implementation of the driving operation for A and B components, respectively, and d to the interaction length of the PO driving operation, with $d = 0$ meaning the absence of the driving operation. (b) Surface excess Γ as a function of the interaction length d . Here, Γ is defined as $1 - \rho_b(L_x - 2\sigma_w)$ with ρ_b the bulk probability density of the colloidal particle.

$\sigma_c = \sqrt[24]{2}\sigma$. Besides the LJ interaction, in order to model rotational diffusion we employ a stick-boundary coupling between the colloidal particle and the solvent, which is implemented by the revised bounce-back rule [18]. We point out that qualitatively similar results can be obtained by using only LJ potential or bounce-back coupling, since the wall-driven diffusioosmotic flow is independent of the colloid-solvent interactions. The interaction between the colloidal particle and the boundary wall is also described by the LJ potential in Eq. (3), but with the interacting length $\sigma_w = 3.7a$ and the corresponding cutoff radius $\sqrt[24]{2}\sigma_w$. This large σ_w ensures that the depletion force due to the existence of solvent particles has no effect [14].

The colloidal particle catalyzes the chemical reaction $A \rightarrow B$ at its surface, and the reactant is simultaneously fed into the solution by performing inverse reaction $B \rightarrow A$ in regions far from the colloidal particle. This produces a concentration gradient of A (and B) around the colloid. Since the colloidal particle has the same interactions with both A and B particles, it cannot feel this chemical gradient. Hence, the colloidal sphere does not experience the diffusiophoresis or self-diffusiophoresis, which allows us to exclusively study the diffusioosmotic effect induced by the boundary wall. The colloidal particle thus performs Brownian motion in the bulk, carrying a stationary concentration profile around it. However, when the colloidal particle approaches the boundary wall, its carried concentration profile will have a significant gradient component parallel to the wall, similar to Fig. 8(a) and (b). This will drive a radially symmetric diffusioosmotic flow with respect to the colloidal particle, and the flow fields are similar to those in Fig. 8(c) and (d). As a consequence, the colloidal particle is pulled to the boundary or pushed away from the boundary by the diffusioosmotic flow, depending on the diffusioosmotic properties of the wall.

Figure 9(a) shows the probability density to find the colloidal particle at a distance from the boundary wall. When the wall generates a diffusioosmotic flow pointing away from the colloid (driving operation applied for

A particles) similar to Fig. 8(c), the compensating flow from the bulk pulls the colloidal sphere toward the wall. Conversely, when the diffusioosmotic flow is toward the colloid (driving operation applied for B particles), a fluid flow pointing inward the bulk is induced similar to Fig. 8(d), and the colloidal sphere is pushed away from the wall. The diffusioosmosis generated by the boundary wall thus leads to an effective attraction or repulsion between the colloidal particle and wall. Due to this purely hydrodynamic effect, the catalytic colloids can show a strong accumulation or depletion at the wall. The magnitude of accumulation or depletion is clearly dependent on the diffusioosmotic intensity, as shown in Fig. 9(b), where the surface excess of the colloidal particle is plotted as the function of the interaction length of the PO driving operation. Through this example, we show that the PO boundary indeed has a significant influence in the motion of active colloids, which cannot be captured by the common stick or slip boundary. Although we here consider a uniformly catalytic colloidal particle, similar behaviors can be expected for self-diffusiophoretic Janus particles.

B. Thermoosmotic boundary

We also apply the mesoscale thermoosmotic boundaries to three different systems, as sketched in Fig. 2(a-c), with a single-component liquid. The system dimensions are the same as their diffusioosmotic counterparts. Unless otherwise stated, the thermoosmotic boundary in this section is type-II (specular reflection plus driving operation), since the type-I boundary leads to a weak thermoosmotic flow.

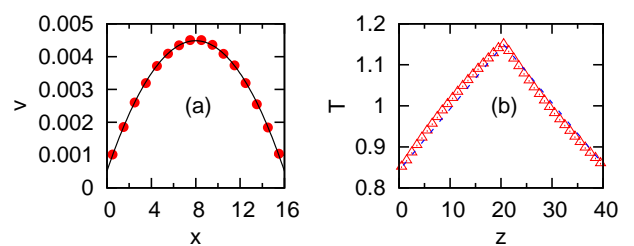


FIG. 10: (a) Poiseuille flow of a homogeneous single-component fluid in a channel with the thermoosmotic boundary. Here, the driving operation is applied for the hot particles with $T_t = 2.5$. The lines correspond to parabolic fits to the flow profile. (b) Steady-state temperature profile in a heterogeneous channel with the thermoosmotic boundary on the left half side. Here we use $d = 0.3$ and $T_t = 0.6$, and perform the driving operation for the cold particles so that the thermoosmotic flow is against the z axis. The dashed lines refer to the temperature distribution in a quiescent fluid.

1. Homogeneous fluid under an external force

The schematic system is shown in Fig. 2(a). In the simulations we use interaction length of $d = 0.5$, the liquid temperature $T = 1.0$, and the driving operation for the hot particle above a threshold temperature $T_t = 2.5$. Under an external force of $g = 0.0001$ per particle, the liquid flows along the z -axis. The stationary velocity profile of the flow field is plotted in Fig. 10(a), which is parabolic with nonzero flow velocity at the wall surface. This is because for the type-II thermoosmotic boundary used in the simulations only the driving operation contributes to the friction, which is not enough to produce a completely no-slip boundary.

2. Inhomogeneous fluid in a heterogeneous channel

The system is displayed in Fig. 2(b), with the thermoosmotic boundary only for the left half of the channel. The symmetric temperature gradient ∇T along the z direction is generated by fixing the temperature at $L_z/2$ and L_z with local thermostats, by which the thermal kinetic energy of local fluid regions are simply rescaled every MPC step. Figure 10(b) shows a steady-state temperature distribution, which only slightly deviates from a linear profile compared to the diffusioosmotic case. This can be understood by noting that the ratio of the characteristic times of the diffusive to convective energy flux is $l_c v / D_T \sim 2 \times 10^{-2}$ with D_T the heat diffusivity, much smaller than the diffusioosmotic counterpart. The resulting stationary fluid flow (not shown) is similar to that in Fig. 4(b) because of the use of the specular reflection at the wall surface. Clearly, the system in Fig. 2(b) can be used as a micropump to transport fluids, in agreement with the previous MD simulation [42], where a symmetric temperature gradient is shown to be able to drive a directed thermoosmotic flow through a channel with heterogeneous wall surfaces.

The velocity of thermoosmotic flow can be tuned by changing ∇T , d and T_t . In Fig. 11 we separately plot the dependence of the thermoosmotic flow velocity on these parameters. Figure 11(a) indicates that this mesoscale scheme correctly reproduces the most fundamental linear relation between the thermoosmotic flow and ∇T , clearly consistent with the existing theoretical predictions [19, 21]. The flow velocity is not sensitive to the interaction length d , as shown in Fig. 11(b), in contrast to the diffusioosmotic case. For fixed ∇T and d , the thermoosmotic flow changes monotonically with T_t , as displayed by Fig. 11(c) and (d). Furthermore, the driving operations implemented for the cold and hot particles generate the thermoosmotic flows in opposite directions, which correspond to opposite thermoosmotic properties. These dependencies can be explained in a way similar to the diffusioosmotic case.

First, note that for the thermoosmotic flows type-II boundary is used, thus both the thermoosmotic and fric-

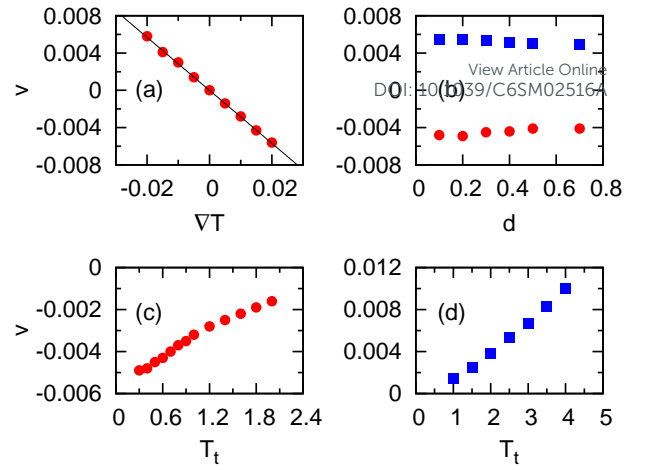


FIG. 11: The thermoosmotic flow velocity as a function of (a) the temperature gradient, (b) the interaction range, (c) and (d) the threshold temperature. Here, the circles and squares refer to the driving operation performed for the cold and hot particles, respectively. The positive direction of the flow velocity is along the z axis. In (a) $d = 0.3$ and $T_t = 0.6$; in (b) $\nabla T = 0.015$, and $T_t = 0.5$ for the cold-particle case and 2.5 for the hot-particle case; in (c) and (d), $d = 0.3$ and $\nabla T = 0.015$.

tional forces arise exclusively from the driving operation. When the driving operation is applied to the cold particles ($E_i < 1.5T_t$), the thermoosmotic force f_T and the frictions depend, respectively, on the diffusive and convective flows of the cold particles within the boundary layer. The thermoosmotic force can be written as $f_T \propto d \nabla c_c$ with c_c being the concentration of the cold particles, and the frictional force is $f_F \sim -d \gamma_D \mathbf{v}$. Here, the friction coefficient per unit thickness γ_D arises from the driving operation of the cold particles and is proportional to c_c . In the steady state $f_T + f_F = 0$, the thermoosmotic flow velocity is determined to be $\mathbf{v} \propto \nabla c_c / c_c$, independent of d , as shown in Fig. 11(b). We can use local equilibrium approximation to evaluate $\nabla c_c / c_c$, despite the temperature inhomogeneity in our system. With the local Maxwellian velocity distribution and ideal gas equation of state, we have $c_c \propto T^{-5/2} \int_0^{3T_t/2} E^{1/2} \exp(-E/T) dE$. Thus, the ratio $\nabla c_c / c_c = (\partial \ln c_c / \partial T) \nabla T$ can be evaluated by numerical integration. The magnitude of the negative prefactor $\partial \ln c_c / \partial T$ monotonically decreases with increasing T_t , in agreement with the simulation result in Fig. 11(c). Similarly, when the driving operations are applied to the hot particles, the thermoosmotic flow velocity is $\mathbf{v} \propto \nabla c_h / c_h = (\partial \ln c_h / \partial T) \nabla T$, with the hot particle concentration $c_h \propto T^{-5/2} \int_{3T_t/2}^{\infty} E^{1/2} \exp(-E/T) dE$. Numerical estimation shows that the positive prefactor $\partial \ln c_h / \partial T$ increases with T_t , consistent with the simulation result in Fig. 11(d).

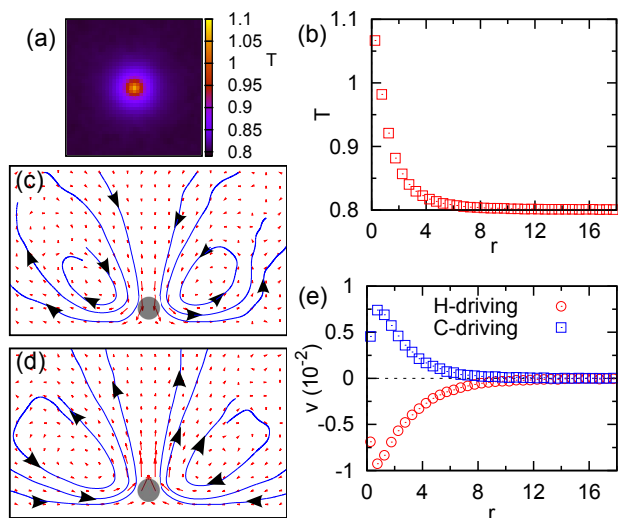


FIG. 12: Temperature and flow fields induced by a heat source close to a wall with the thermoosmotic boundary condition. (a) Temperature map on the plane of $x = 1.0$ and (b) the corresponding temperature as a function of the in-plane distance to the heat source center. (c) and (d) are the flow fields on the xz plane across the source center, with the driving operation respectively applied for the cold particles (thermophilic) and the hot particles (thermophobic). (e) Flow velocity on the plane of $x = 1.0$, with the squares and circles corresponding to the flows in (c) and (d), respectively.

3. Inhomogeneous fluid driven by a single wall

Parallel to the diffusioosmotic case, we investigate the thermoosmotic flow fields induced by a spherical high-temperature region near the wall, as sketched in Fig. 2(c). The active fluid region heats up the surrounding fluid and generates a radially symmetric temperature gradient on the x plane. In order to maintain a steady-state temperature distribution, the input energy is drained from the system through the wall with a lower temperature. In the simulation, the hot active region of temperature $T_s = 1.3$ is imposed by rescaling its thermal energy; while the cold wall of $T_w = 0.8$ is realized by using the stochastically thermalized stick wall [17, 46, 48], which leads to a stick-like boundary. Since the wall has a constant temperature, the temperature inhomogeneity of the fluid nearest the wall is weak. To generate a large thermoosmotic flow, we choose the effective wall-fluid interaction region as $0.5 < x < 1.5$, in which the temperature gradient parallel to the wall is relatively strong. The thermophobic and thermophilic walls are modeled respectively by implementing the driving operation for the hot particles with $T_t = 2.5$ and for the cold particles with $T_t = 0.8$, which produce opposite thermoosmotic flows.

Figure 12(a) and (b) show the stationary temperature distribution in the plane of $x = 1.0$. Comparing with the chemical gradient in Fig. 8(a) and (b), the temperature gradient decays much fast, since the bottom wall is a constant-temperature heat sink instead of adiabatic

boundary. The temperature gradient-induced flow fields are plotted in Fig. 12(c) and (d), whose patterns are similar to those of the diffusioosmosis. The thermoosmotic flows are shorter-ranged due to the fast decay of thermal gradient, as shown in Fig. 12(e). When the driving operation is applied to the cold particles, the thermoosmotic flow near the wall points outwards from the active region, consistent with a thermophilic wall; otherwise the thermoosmotic flow reverses, corresponding to a thermophobic wall. Although in the present configuration the thermoosmosis-induced flow field is relatively short-ranged, it can be expected to significantly influence colloidal dynamics in the presence of large local thermal gradients, as in the cases of hot Brownian particles [53] or self-thermophoretic Janus particles [18, 25, 28, 54–56]. Here, the effect of the thermoosmotic wall on the active colloidal particle will be similar to that in the diffusioosmotic counterpart.

We finally emphasize that the simulation system in Fig. 12 is quite similar to that of a very recent experiment [57]. In that work, a thermoosmotic flow is induced along a water-glass boundary due to a radially symmetric temperature gradient that is generated by a heated Au nanoparticle immobilized at the glass surface. The observed flow field is consistent with our simulation result in Fig. 12(d), since the glass material used in the experiment is thermophobic.

V. CONCLUSIONS

In this work, we propose a mesoscopic simulation scheme to implement the PO boundary conditions. Based on the widely used coarse-grained no-slip/slip boundary conditions, the PO boundary is achieved by introducing a driving operation within a boundary layer, that simply reverses the tangential velocity of fluid particles of a selected type. In homogeneous fluids, the driving operation only contributes to additional friction; while in gradient-induced inhomogeneous fluids, the driving operation together with the nonzero diffusive flux of the selected particles lead to a net PO force. Because the instantaneous driving operation is completely compatible with the particle-based fluid, the proposed PO boundaries can be well applied in all the particle-based mesoscale simulations, including lattice Boltzmann, DPD or MPC. We justify the mesoscopic simulation scheme by implementing both the diffusioosmotic and thermoosmotic boundary conditions, where the fluid particles are classified according to particle species or kinetic energy, respectively. The proposed scheme correctly reproduces the well-known linear relation between the PO flow and the applied gradient, directly arising from the coarse-grained fluid-wall interactions, and all the simulation results can be qualitatively explained by theory. The direction and magnitude of the PO flow can be flexibly tuned by adjusting the fluid-wall coupling, which can mimic a wide range of combinations of the wall materials and flu-

id compositions. More importantly, the implementation of the mesoscale PO boundaries is simple and efficient enough to perform large-scale fluid simulations. As applications, we use this mesoscale scheme to simulate the PO transport of fluids in various microfluidic environments. Furthermore, we use it to study the effect of a diffusioosmotic boundary wall on the motion of a catalytic colloidal particle, which shows that the diffusioosmosis can produce a significant hydrodynamic accumulation or depletion of the colloidal particle at the wall. Our work thus paves the way for investigating the important effect of the PO boundaries on nonequilibrium structure and

dynamics in complex fluids by mesoscale simulations.

View Article Online
DOI: 10.1039/C6SM02516A

Acknowledgments

We thank Marisol Ripoll for helpful discussions. We gratefully acknowledge support from National Natural Science Foundation of China (Grant No. 11404379, 11674365, 11474327). This work was also supported by the MOST 973 Program (No. 2015CB856800).

- [1] J. K. G. Dhont, *An Introduction to Dynamics of Colloids* (Elsevier, 1996).
- [2] M. Doi and S. F. Edwards, *The Theory of Polymer Dynamics* (Oxford University Press, Oxford, 1986).
- [3] S. Succi, *The Lattice Boltzmann Equation: for fluid dynamics and beyond* (Clarendon, Oxford, 2001).
- [4] G. A. Bird, *Molecular Gas Dynamics* (Clarendon, Oxford, 1976).
- [5] F. J. Alexander and A. L. Garcia, *Comp. in Phys.* **11**, 588 (1997).
- [6] P. J. Hoogerbrugge and J. M. V. A. Koelman, *Europhys. Lett.* **19**, 155 (1992).
- [7] P. Espanol and P. B. Warren, *Europhys. Lett.* **30**, 191 (1995).
- [8] C. P. Lowe, *Europhys. Lett.* **47**, 145 (1999).
- [9] A. Malevanets and R. Kapral, *J. Chem. Phys.* **110**, 8605 (1999).
- [10] R. Kapral, *Adv. Chem. Phys.* **140**, 89 (2008).
- [11] G. Gompper, T. Ihle, D. M. Kroll, and R. G. Winkler, *Adv. Polym. Sci.* **221**, 1 (2009).
- [12] L. Bocquet and J.-L. Barrat, *Soft matter* **3**, 685 (2007).
- [13] A. Malevanets and R. Kapral, *J. Chem. Phys.* **112**, 7260 (2000).
- [14] J. T. Padding and A. A. Louis, *Phys. Rev. E* **93**, 031402 (2006).
- [15] M. Yang, M. Theers, J. Hu, G. Gompper, R. G. Winkler, and M. Ripoll, *Phys. Rev. E* **92**, 013301 (2015).
- [16] A. Lamura, G. Gompper, T. Ihle, and D. M. Kroll, *Europhys. Lett.* **56**, 319 (2001).
- [17] J. T. Padding, A. Wysocki, H. Löwen, and A. A. Louis, *J. Phys.: Condens. Matter* **17**, S3393 (2005).
- [18] M. Yang, A. Wysocki, and M. Ripoll, *Soft Matter* **10**, 6208 (2014).
- [19] J. L. Anderson, *Annu. Rev. Fluid Mech.* **21**, 61 (1989).
- [20] R. J. Hunter, *Foundations of Colloid Science* (Oxford University Press, New York, 1991).
- [21] A. Würger, *Rep. Prog. Phys.* **73**, 126601 (2010).
- [22] S. Michelin, T. D. Montenegro-Johnson, G. De Canio, N. Lobato-Dauzier, and E. Lauga, *Soft Matter* **11**, 5804 (2015).
- [23] W. F. Paxton, K. C. Kistler, C. C. Olmeda, A. Sen, S. K. S. Angelo, Y. Cao, T. E. Mallouk, P. E. Lammert, and V. H. Crespi, *J. Am. Chem. Soc.* **126**, 13424 (2004).
- [24] J. R. Howse, R. A. L. Jones, A. J. Ryan, T. Gough, R. Vafabakhsh, and R. Golestanian, *Phys. Rev. Lett.* **99**, 048102 (2007).
- [25] H. R. Jiang, N. Yoshinaga, and M. Sano, *Phys. Rev. Lett.* **105**, 268302 (2010).
- [26] G. Rückner and R. Kapral, *Phys. Rev. Lett.* **98**, 150603 (2007).
- [27] L. F. Valadares, Y. G. Tao, N. S. Zacharia, V. Kitaev, F. Galembeck, R. Kapral, and G. A. Ozin, *Small* **6**, 565 (2010).
- [28] M. Yang and M. Ripoll, *Phys. Rev. E* **84**, 061401 (2011).
- [29] M. Yang and M. Ripoll, *Soft Matter* **10**, 1006 (2014).
- [30] M. Yang, M. Ripoll, and K. Chen, *J. Chem. Phys.* **142**, 054902 (2015).
- [31] J. Palacci, S. Sacanna, A. P. Steinberg, D. J. Pine, and P. M. Chaikin, *Science* **339**, 936 (2013).
- [32] W. Duan, R. Liu, and A. Sen, *J. Am. Chem. Soc.* **135**, 1280 (2013).
- [33] S. Das, A. Garg, A. I. Campbell, J. Howse, A. Sen, D. Velegol, R. Golestanian, and S. J. Ebbens, *Nature communications* **6** (2015).
- [34] W. E. Uspal, M. N. Popescu, S. Dietrich, and M. Tasinkevych, *Phys. Rev. Lett.* **117**, 048002 (2016).
- [35] J. Simmchen, J. Katuri, W. E. Uspal, M. N. Popescu, M. Tasinkevych, and S. Sánchez, *Nature communications* **7**, 10598 (2016).
- [36] T. M. Squires and S. R. Quake, *Rev. Mod. Phys.* **77**, 977 (2005).
- [37] V. Yadav, H. Zhang, R. Pavlick, and A. Sen, *J. Am. Chem. Soc.* **134**, 15688 (2012).
- [38] J. J. McDermott, A. Kar, M. Daher, S. Klara, G. Wang, A. Sen, and D. Velegol, *Langmuir* **28**, 15491 (2012).
- [39] A. Siria, P. Poncharal, A.-L. Biance, R. Fulcrand, X. Blase, S. T. Purcell, and L. Bocquet, *Nature* **494**, 455 (2013).
- [40] A. Ajdari and L. Bocquet, *Phys. Rev. Lett.* **96**, 186102 (2006).
- [41] D. M. Huang, C. Cottin-Bizonne, C. Ybert, and L. Bocquet, *Phys. Rev. Lett.* **101**, 064503 (2008).
- [42] C. Liu and Z. Li, *Phys. Rev. Lett.* **105**, 174501 (2010).
- [43] M. Yang and M. Ripoll, *Soft Matter* **12**, 8564 (2016).
- [44] M. Shen, F. Ye, R. Liu, K. Chen, M. Yang, and M. Ripoll, *J. Chem. Phys.* **145**, 124119 (2016).
- [45] M. J. Huang, J. Schofield, and R. Kapral, *Soft Matter* (2016).
- [46] J. L. Lebowitz and H. Spohn, *J. Stat. Phys.* **19**, 633 (1978).
- [47] Y. Inoue, Y. Chen, and H. Ohashi, *J. Stat. Phys.* **107**, 85 (2002).

- [48] M. Hecht, J. Harting, T. Ihle, and H. J. Herrmann, *Phys. Rev. E* **72**, 011408 (2005).
- [49] T. Ihle and D. M. Kroll, *Phys. Rev. E* **63**, 020201(R) (2001).
- [50] D. J. Tritton, *Physical Fluid Dynamics* (Oxford Science publications, 1988), 2nd ed.
- [51] C. Huang, A. Chatterji, G. Sutmann, G. Gompper, and R. G. Winkler, *J. Comput. Phys.* **229**, 168 (2010).
- [52] E. Tüzel, T. Ihle, and D. M. Kroll, *Phys. Rev. E* **74**, 056702 (2006).
- [53] D. Rings, R. Schachoff, M. Selmke, F. Cichos, and K. Kroy, *Phys. Rev. Lett.* **105**, 090604 (2010).
- [54] B. Qian, D. Montiel, A. Bregulla, F. Cichos, and H. Yang, *Chemical Science* **4**, 1420 (2013). View Article Online
- [55] S. Simoncelli, J. Summer, S. Nedev, P. Kühler, and J. Feldmann, *Small* **12**, 2854 (2016). DOI: 10.1039/C6SM02516A
- [56] D. A. Fedosov, A. Sengupta, and G. Gompper, *Soft Matter* **11**, 6703 (2015).
- [57] A. P. Bregulla, A. Würger, K. Günther, M. Mertig, and F. Cichos, *Phys. Rev. Lett.* **116**, 188303 (2016).